DOI: 10.1021/ma100496g

Macromolecules
COMMUNICATION TO THE EDITOR

A New Scenario of Flow-Induced Shish-Kebab Formation in Entangled Polymer Solutions

Takeji Hashimoto,*,†,§,⊥ Hiroki Murase,*,†,‡ and Yasuo Ohta*,‡

†*Department of Polymer Chemistry, Graduate School of Engineering, Kyoto University, Katsura, Nishikyo-ku, Kyoto 615-8510, Japan,* ‡*Research Center, TOYOBO Co., Ltd., 2-1-1 Katata, Ohtsu-shi, Shiga 520-0292, Japan, and* §*Advanced Science Research Center (ASRC), Japan Atomic Energy Agency (JAEA), Tokai-mura, Naka-gun, Ibaraki 319-1195, Japan,* ⊥Professor Emeritus, Kyoto University, Japan

Received March 4, 2010
Revised Manuscript Received July 20, 2010

Introduction. Since the first reports of shish-kebab by about 50 years ago,[1,2] its formation mechanism has been investigated to this date on the basis of *the flow-induced crystallization phenomenon*.[3] Nevertheless, detailed kinetic pathways leading to the shish-kebab formation have not yet been fully clarified. Its investigation has now been one of the extremely hot research themes.[4−15] Under this current stream it may be of worthy to present our recent discovery of a new scenario about the kinetic pathways for a specific system of *polymer solutions* of entangled ultrahigh molecular weight (UHMW) linear polyethylene (UHMWPE). We would like to emphasize here the fact that our work focuses on much earlier stages of the kinetic pathways than the stages investigated by those previous works described above. In short, our works elucidated the stages before the flow-induced upturn in birefringence starts being discerned in the systems, whereas most of the previous works focused only on the stages after onset of the birefringence upturn.

We would like to emphasize also that the crystallizable, entangled polymer solutions to be discussed here belong to the so-called dynamically asymmetric systems[16−18] in which external fields imposed on the systems bring about the flow-induced concentration fluctuations[19−24] and *flow-induced liquid−liquid phase separation*.[25] How are these effects coupled with the flow-induced crystallization? Surprisingly, *the coupling effects* have been left almost unexplored up to now in this research field, except for the work of McHugh and co-workers,[26−29] who suggested the flow-induced phase separation preceding the flow-induced crystallization in *dilute polymer solutions*. This is because the flow-induced phase separation occurs prior to the crystallization, and the flow-induced phase-separated structures can be observed only in situ, as the flow-induced phase-separated structures decay rapidly and hence cannot be observed after the cessation of the flow. The same phase separation may occur in sheared binary melt blends of UHMW and low molecular weight (LMW) polymers having the same monomeric units, again mediated by the dynamic asymmetry and the stress-diffusion coupling.[16−18] However this phase separation, even if it occurred, cannot be observed because of no refractive index (n) or electron density difference between the two components and hence between the two phases, if the LMW component has a molecular weight larger than the critical molecular weight, above which n or mass density reaches a constant value independent of the molecular weight. These facts may have led us to overlook important roles of the phase separation on the shish-kebab formation up to today.

Results and Discussion. We investigated a time evolution of isothermal self-assembling processes of a UHMWPE solution (in paraffin as a solvent with concentration $c = 10c^*$, as described in detail in Appendix 1) induced by the simple shear flow at 124 °C after a step-up shear from shear rate $\dot{\gamma} = 0$ to a high shear rate $\dot{\gamma} = 2.9\ s^{-1} > \dot{\gamma}_a = 1.2\ s^{-1}$, the critical shear rate for the formation of optically anisotropic string-like structures.[30] The $\dot{\gamma}_a$ was found[31] to be approximately equal to the inverse of chain retraction time $\tau_e = 2\tau_R$, τ_R being the longest Rouse time.[32,33] The quiescent solutions at 124 °C are *thermodynamically stable and homogeneous*, involving no crystallization and no phase separation at all, because the nominal melting temperature of crystals in the quiescent solution is 115−119 °C, depending on crystallization conditions.

Figure 1A typically demonstrates online snapshots of time evolution of optical microscope images (OM) *a1* to *a4* after the step-up shear described above and the snapshot *a5* taken immediately after the shear cessation from stage 2 (to be described in detail later). The corresponding sketches are shown in *b1* to *b4*, while *b5* is the TEM image taken after cooling the shear-ceased solutions. Here the x-, y-, and z-axes are taken parallel to the flow, velocity gradient, and neutral (or vorticity) directions, respectively. These OM images were simultaneously recorded with small-angle light scattering (SALS), birefringence $\Delta n_{x-z}(t)$, and stress $\sigma(t)$ shown in Figure 1B, the details of which were described in Appendices 2 and 3. Observed spatial brightness variations in these OMs represent the concentration fluctuations developed in the sheared solution because the fast Fourier transforms of the OMs effectively reproduce the characteristics of the SALS patterns. All these results indicate that the entire time-evolution process can be classified into the four fundamental processes occurring in the time regions t_1 to t_4 as also indicated in Figure 1, though region t_1 is not included in Figure 1A.

In region t_1 where time $t < t_{c1}$, t_{c1} being the so-called "solvent-squeezing time" found for the noncrystallizable polymer solutions,[18,34,35] the OM image and the SALS cannot be clearly discerned so that the sheared solution remains essentially homogeneous. This is the reason why the OM image and the SALS pattern are not shown in this time region. It should be also noted that, in time region 1, the integrated scattered intensity $\mathcal{I}_\parallel(t)$ and $\mathcal{I}_\perp(t)$ are equal to $\mathcal{I}_\parallel(t = 0) = \mathcal{I}_\perp(t = 0)$ for the quiescent solution and that the SALS pattern 1 in Figure 1B belongs to time region t_2 but not t_1. This infers that the entangled chains are more or less uniformly deformed, causing stress up-rise with time up to $t \simeq \sim 1$ s in the first stress overshoot process as shown in part B and as described in Appendix 3.

In region t_2 where $t_{c1} \leq t < t_{c2}$, t_{c2} being the characteristic time for formation of the demixed domains,[35] we discerned the OM image *a1* which essentially represents the plane-wave-type concentration fluctuations with their wave vectors oriented along the x-axis as indicated by the sketch in

*Corresponding authors. E-mail: hashimoto@alloy.polym.kyoto-u.ac.jp (T.H.), hiroki_murase@toyobo.jp (H.M.), yasuo_ohta@toyobo.jp (Y.O.).

 Published on Web 07/27/2010

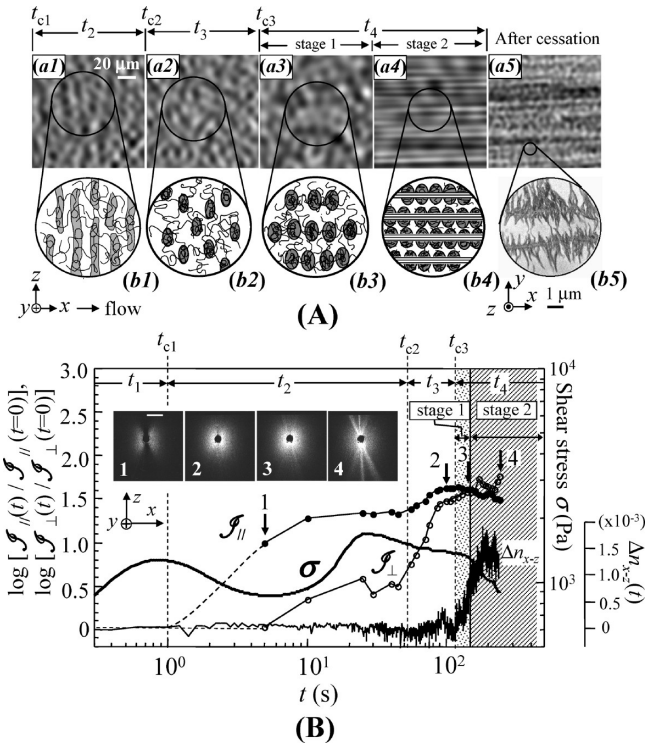

Figure 1. (A) Online snapshots of OM images (*a1*) to (*a4*) after the step-up shear from $\dot{\gamma} = 0$ to $\dot{\gamma} = 2.9\ s^{-1}$ and at 124 °C and the corresponding sketches (*b1*) to (*b4*): the snapshot (*a5*) taken at 124 °C immediately after the shear cessation and the corresponding TEM (*b5*) taken after cooling the solution. The white bar is common to all the images except for (*b5*). (B) Time evolution of shear stress $\sigma(t)$ (right ordinate axis), birefringence $\Delta n_{x-z}(t)$ (rightmost ordinate axis), integrated SALS intensity parallel (along *x*-axis), and perpendicular (along *z*-axis) to the flow direction (left ordinate axis), $\mathscr{I}_{\parallel}(t)$ and $\mathscr{I}_{\perp}(t)$, respectively, normalized with the integrated intensity for the quiescent solution at time $t = 0$, and online snap shots of SALS patterns taken at representative times (time regions t_2, t_3, t_4(stage 1), and t_4(stage 2)) as indicated by the arrows numbered 1−4 on the top of the $\mathscr{I}_{\parallel}$ in (B). All of these also were simultaneously measured together with the OM images after the step-up shear from $\dot{\gamma} = 0$ to $\dot{\gamma} = 2.9\ s^{-1}$ and at 124 °C. The white bar in pattern 1 corresponds to $q = 5.2 \times 10^{-4}\ nm^{-1}$ and is common to all other SALS patterns. The Cartesian coordinate axes, *x*-, *y*-, and *z*-axis in (A) and (B) correspond to flow, velocity gradient, and neutral (vorticity) axes, respectively. All the OM images were taken at the shutter speed of 10^{-4} s.

part *b1*, where the shaded and unshaded regions represent those rich and poor in polymers, respectively. The average spacing of the waves is ∼16 μm. The physical origin for formation of the plane-wave-type concentration fluctuations is discussed in Appendix 3.

In region t_3 where $t_{c2} \le t < t_{c3}$, t_{c3} being the characteristic time for the string formation,[30,34] the image *a2* suggests formation of the demixed domains whose centers are randomly distributed in space, as sketched in *b2*. This is supported by both the SALS pattern 2 and the scattered intensity $\mathscr{I}_{\parallel}$ and $\mathscr{I}_{\perp}$ (part B) as well. As total strain $\dot{\gamma}t$ increases in region t_2, the amplitude of the plane-wave concentration fluctuations increases, as evidenced by the increased SALS intensity along the flow direction $\mathscr{I}_{\parallel}$ with *t*, so that hydrodynamic effects on the polymer-rich region increase and eventually destabilize the fluctuations and transform them into the demixed domains. This process may involve the second overshoot of $\sigma(t)$ as seen in Figure 1B.

In region t_4 where $t \ge t_{c3}$, the demixed domains are aligned into the stringlike assemblies oriented parallel to the flow direction, as shown in images *a3* and *a4* and in sketches *b3* and *b4*. In the strings, the mass centers of the demixed domains are nematically aligned parallel to the flow direction. However, the birefringence is almost zero up to time region 3 and is still small in stage 1 in time region 4 as evidenced in part B, so that polymer chains themselves are essentially in random coils even under the flow. It should be stressed that almost all the previous works have not either focused on or fully explored the time evolution of the shear-induced self-assembly in these time regions (from region t_2 to stage 1 in region t_4) before the birefringence upturn is clearly discerned. However, we discovered that the important dissipative structures, as shown by sketches *b1*−*b3* in part A, have been already developed in these time regions.

The observed drastic increase in birefringence in region t_4 in part B leads us to further classify this region into two stages across the vertical solid line shown in Figure 1B: stage 1 where birefringence becomes slightly positive so that the strings have only a weak birefringence; stage 2 where birefringence sharply increases with time, which reveals that bundles of stretched chains interconnecting the demixed domains may start to be formed parallel to the string as illustrated by straight lines in the sketch *b4*, thereby the string starts to have a strong optical anisotropy. It is in this stage 2 that we can observe a signature for the shear-induced crystallization (see Appendix 3 for details).

The alignments of the domains in stage 1 will be driven again by the hydrodynamic effects, which will entrap the off-aligned domains into the strings, causing a densification of the domains in the assembly with time and eventually formation of chains bridging the neighboring domains. These chains may be stretched into the bundles of oriented chains under the flow. The alignments of the domains will effectively reduce the stress level at the large $\dot{\gamma}t$ in time region t_3. The bundles thus created will grow toward the interior of the domains as sketched in *b4* and as will be suggested later in conjunction with Figure 3c.

It is striking to note that the OM image *a5* did not disappear even after the shear cessation and that the streak-like SALS pattern further increased in its intensity with time[30] even after the shear cessation. These results indicate that crystallization occurred in situ under the shear flow in stage 2 and that this crystallization not only prevents relaxation of the shear-induced structures but also promotes further a seeded crystallization even after the shear cessation, according to the mechanism proposed by Peterman and coworkers.[36] The TEM image shown in *b5* in part A clearly reveals formation of the shish-kebab morphology, though it may be grown also during the cooling process of the solution for TEM observations (see Appendix 2). Nevertheless, we believe that the pieces of experimental evidence obtained suggest that the optically anisotropic stringlike self-assembly serves as a precursor of shish-kebabs and that models *b1* to *b4* unveil a series of kinetic pathways leading to shish-kebab formation in the sheared solutions.

We would like to further reinforce universality of our scenario through investigations of the structure formation along the fiber spinning line. Here the *thermodynamically stable, homogeneous solution* is subjected to the shear and elongational flow, a relative weight of which depends on the position along the spinning line from the spinneret. Figure 2a shows a typical TEM image for the fiber sampled at position A shown later in Figure 3e. In the image, the polymer-rich domains appear dark, while the solvent-rich matrix phase appears bright (Appendix 2). The TEM image reveals that the polymer-rich domains are extended perpendicular to the fiber axis and their mass centers are randomly aligned in

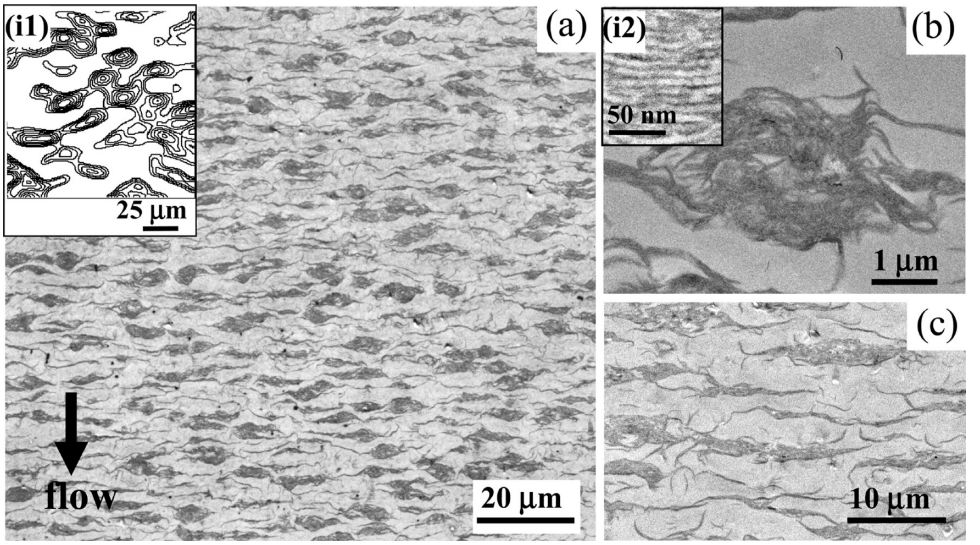

Figure 2. TEM images of the fiber sampled at 30 mm down stream from the spinneret (position A in Figure 3e): (a) a low-magnification image; (b) a zoom-in image of the demixed domains in (a); (c) a zoom-in image of a local region rich in solidified plane-wave-type concentration fluctuations. The inset to (a) (image *i1*) shows a contour pattern of the isointensity lines for the spatial brightness distribution of the online snapshot of image *a2* in Figure 1. The inset to (b) (image *i2*) shows a zoom-in image of lamellae comprising the demixed domain. All the images were stained by RuO_4. The arrow in (a) indicates the flow direction (or the fiber axis) common to all the images.

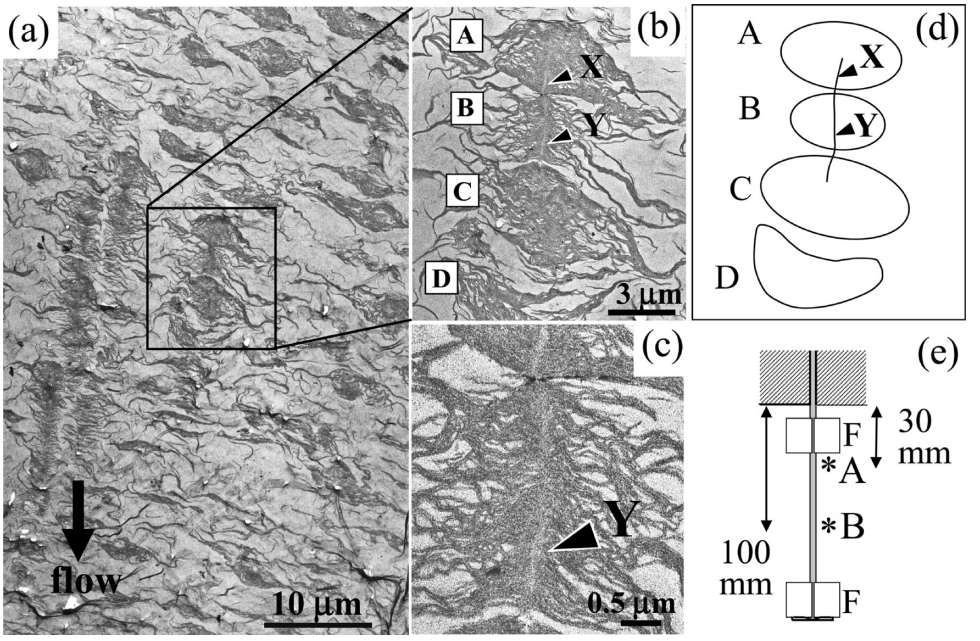

Figure 3. TEM images of the fiber sampled at 100 mm down stream from the spinneret (position B): (a) a low-magnification image, (b) a zoom-in image of the region encompassed by the black line in part (a), (c) a zoom-in image of the demixed domain B in (b), (d) a schematic illustration of the image in (b), and (e) a schematic illustration of a part of the fiber which runs through the spinning line and which was cut out and fixed by the frame F (a cross-sectional view). *A and *B specify the positions for the TEM observations which respectively locate at 30 and 100 mm down stream from the spinneret. The arrow indicates the flow direction or the fiber axis common to all the images.

space. These flow-induced structures are quite similar to those shown by the online snapshot *a2* and its isointensity contour plot shown in the inset image *i1*.[37] The average domain size and interdomain distance observed in the TEM and OM are roughly the same. Figure 2b, which focuses on the polymer-rich domain itself, elucidates that the lamellar crystallization, occurring in the demixed domains during the cooling process of the specimen, served for the solidification of the demixed domains, as described in Appendix 2.

The TEM image in the upstream side of the spinneret showed the dark wavelike domains as highlighted in Figure 2c. We believe they reflect a memory of the plane-wave-type concentration fluctuations, as shown in *a1* and *b1* in Figure 1A, which was solidified by the lamellar crystallization during the cooling process of the specimen for the TEM observations.

Figure 3a shows the TEM image of the fiber sampled at position B (see the sketch in part e). The image reveals self-assemblies of the polymer-rich domains aligned parallel to the spinning line, essentially similar to the strings observed in the online snapshots shown by *b3* in Figure 1A.[37] The image in part b was obtained by zooming in an assembly of the four demixed domains, A to D, encompassed by the dark square in part a. We can observe formation of a shish passing through the points X and Y, which appears bright as it cannot be

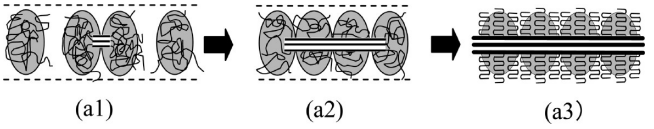

Figure 4. Proposed new scenario for nucleation growth of shish-kebabs. The flow direction is horizontal.

stained with RuO_4, as sketched in part d by a line. The trend described above is more clearly seen in the zoom-in image of the demixed domain B (part c). The shishs appear to start developing in the domain boundaries between B and A and between B and C. They appear to grow toward the interior of domain B and finally tend to be interconnected within the domain B. They tend to grow also toward the inside of the domains A and C.[40] The growth may involve the mechanism proposed by Peterman and co-workers.[36] We believe that this kind of structure is really a prototype of the shish-kebab, as it shows up the shish and the epitaxially overgrown lamellae having a long period of ~10 nm within the demixed domains.

A new scenario proposed here comprises a series of kinetic pathways as schematically shown in sketches *b1* to *b4* in Figure 1A and partially in Figure 4. In the new scenario, the demixed domains in the strings play the following important roles: (1) The domains create bundles of stretched chains from their boundaries which then grow toward the interiors of the demixed domains as evidenced by Figure 3c and modeled by *a1* and *a2* in Figure 4;[40] (2) Formation of the bundles interconnecting the domains results in nucleation−growth of shishs and then the epitaxial growth of the kebabs from the shishs as illustrated by a3 in Figure 4; (3) The domains serve as reservoirs for random coils, in which kebabs are efficiently formed from the shishs. Thus, we conclude that the phase separation mediated by the dynamic asymmetry of the component molecules and the stress−diffusion coupling provide a key for the kinetic pathways leading to shish-kebab formation from the concentrated solutions. It is also important to note that the nature creates shish-kebabs from entangled polymer solutions subjected to the flow via the *complex but rational* kinetic pathways as elucidated in this work. It should be noted that the observation reported and the model presented here are restricted to the special system (solutions of entangled UHMW polymers) at this stage. The generalization of the observed effects and the proposed model for binary melt blends of UHMW and LMW polymers having the same monomeric units and for polymers having large MW polydispersity in melt deserve future works.[41] Finally, we would like to stress again that the flow-induced phase separation is quite general for the dynamically asymmetric polymer systems (solutions or mixtures) having the large asymmetric parameter.[16,42] Hence, at least if one of the components in the systems is crystallizable, the flow-induced phase separation before the flow-induced crystallization must be quite general, under the condition that the systems in quiescent state are stable so that they involve neither crystallization nor phase separation.

Appendix 1. Materials

The polymer used is an ultrahigh molecular weight linear polyethylene (UHMWPE) having weight-average molecular weight $M_w = 2.0 \times 10^6$ and heterogeneity index $M_w/M_n = 12$, where M_n is number-average molecular weight. The typical concentrated polymer solutions studied had concentration $c = 5.0$ wt % ($c/c^* = 10$) in paraffin, as a solvent, having melting temperature $T_m = 69$ °C, and $M_n \sim 500$, where c^* is the overlap concentration,[43] or $c = 10.0$ wt % in decalin ($c/c^* = 20$). The concentrated UHMWPE solutions were prepared by mixing UHMWPE, the solvent (paraffin or decalin), and an antioxidant agent (2,6-di-*tert*-butyl-*p*-cresol), by an amount of 1 wt % of the total solution, at 210 °C by using a twin screw extruder. Small particles contaminating the solutions were filtered off by a mesh filter (400 lines/in.). This process is very important to obtain good light scattering data, simply because intense parasitic scattering arising from the particles will obscure the weak genuine scattering from the concentrated solutions having a small refractive index increment ($\partial n/\partial c$).[44]

Appendix 2. Methods

The flow-induced structure formation in the thermodynamically stable and homogeneous UHMWPE solutions in the absence of flow was studied in two ways. One involves online, real-time, and simultaneous observations of small-angle light scattering (SALS), transmission optical microscopy (OM), birefringence, shear stress, and normal stress of the paraffin solutions at 124 °C well above the nominal melting temperature 115−119 °C for the quiescent solution under the simple shear flow by using the rheo-optical apparatuses constructed in our laboratory[45,46] which utilizes an optically transparent cone-and-plate shear cell. The other involves off-line observations of the superstructures of UHMWPE developed along the fiber spinning lines with transmission electron microscopy (TEM).

The fiber spinning process involves an extrusion of the homogeneous decalin solutions prepared by a twin extruder through the spinneret, having an orifice diameter of 0.8 mm and controlled at 170 °C, with the throughput rate of 1 g/min. The extrudates were cooled down by the nitrogen gas at room temperature, while they were drawn into fibers with a take-up velocity of 60 m/min.

In order to explore crystalline superstructures developed along the fiber spinning line, a part of the fiber running through the spinning line was quickly sampled out from the spinning line into a frame having razor blades at its upper and lower edges of the frame to cut out the running fibers from various positions along the spinning line. The specimen fixed by the frame was quickly quenched to room temperature with a nitrogen gas flow for solidification. This solidification process involves a further advance in crystallization from the crystallized state attained in situ in the spinning line.

The specimen taken out from the spinning line is gel-like and hence containing the solvent as much as 90 wt %, which must be completely removed before TEM observations without changing the structure developed in the as-sampled spun fibers. For this purpose the solvent was first exchanged to acetone at room temperature by repeating a stepwise soaking of the specimen into an acetone/decalin mixture, in which the composition of acetone/decalin was stepwisely changed from 10/90 to 100/0 w/w. Acetone was then exchanged to epoxy monomer by using the same solvent exchange procedure as described above. The specimen was then solidified by curing epoxy monomer into epoxy resin at 60 °C for ~8 h. The solvent-exchange process and the curing process were confirmed to hardly affect the structure developed in the cooled fibers by the observations of light scattering patterns and OM images being essentially unaltered before and after the processes, as detailed elsewhere.[47]

A block of the epoxy resin, in which the fibers are embedded, was trimmed to expose the inner region of the fiber for staining with RuO_4 vapor for 10 h at room temperature. The stained specimen was cut into ultrathin sections of ~80 nm in thickness parallel to the fiber axis with a diamond knife mounted on an ultramicrotome (Ultratome V, LKB Co.Ltd.) at room temperature. The sliced sections were prepared in such a way that they contain the central part of the fiber in the middle of them and mounted on carbon-coated poly(vinyl formal) film on copper

grids for TEM observation with JEM-200CX (JEOL,Tokyo, Japan) operated at 100 kV.

TEM images, as shown in part *b5* in Figure 1A, observed for the solution after the cessation of shear were taken as follows. Immediately after the cessation, the solution was quenched and solidified, together with the shear cell, into an ice water bath. The solidified, gel-like solution was taken out from the shear cell. The solidification process involves a further advance in crystallization in the shear-ceased solutions in such a sense as described above for the fiber specimen. A small piece of a rectangular parallelepiped specimen was cut out from the solidified gel. The piece was trimmed and immersed in liquid paraffin at 79 °C for 1 h under a gentle agitation in order to exchange paraffin to liquid paraffin. Liquid paraffin was then exchanged stepwisely into propylene oxide, which was finally exchanged to epoxy monomers with the same stepwise solvent-exchange procedure employed for the fiber specimens as described above. The rest of the procedures taken for TEM observations are the same as those described above for the fiber specimens. Ultarathin sections of the thickness ~70 nm were cut parallel to *xy*-plane (the plane parallel to the flow direction and velocity gradient direction). We verified that the solvent-exchange procedures employed for this system also do not cause any significant change in their internal structures by investigating them before and after the solvent exchanges with OM and SALS.[47]

SALS pattern and intensity distributions under the simple shear flow were measured at real time by sending incident beam along the velocity gradient direction (*y*-axis parallel to the rotational axis of the shear cell) with a CCD camera. The integrated scattered intensity parallel (along the *x*-axis) and perpendicular (along the *z*-axis) to the flow direction were measured as a function of time t after a step up shear from shear rate $\dot{\gamma} = 0$ to $\dot{\gamma}$.

$$\mathcal{I}_{\parallel}(t) = \int_{a1}^{a2} \mathrm{d}q_x \int_{-\delta}^{\delta} \mathrm{d}q_z \, I(q_x, q_z; t)$$

$$\mathcal{I}_{\perp}(t) = \int_{a1}^{a2} \mathrm{d}q_z \int_{-\delta}^{\delta} \mathrm{d}q_x \, I(q_x, q_z; t)$$

where $I(q_x,q_y,q_z)$ is the scattered intensity at time t after the step-up shear where q_j ($j = x, z$) is the jth component of the scattering vector **q** whose magnitude is defined by

$$q = (4\pi/\lambda)\sin(\theta/2)$$

with θ and λ being scattering angle and wavelength of light in the sample solution. The values a_1, a_2, and δ were set equal to 1.77×10^{-4} nm^{-1}, 1.80×10^{-3} nm^{-1}, and 1.10×10^{-4} nm^{-1}, respectively.

Appendix 3. Simultaneous Online Observations of Rheo-Optical Properties during Structural-Evolution Processes into a Precursor of Shish-Kebabs

Figure 1A,B typically demonstrates and summarizes the time evolution of various quantities simultaneously measured after the onset of the step-up shear to a very high shear rate at $\dot{\gamma} > \dot{\gamma}_a \sim \tau_e^{-1}$,[31] where τ_e is the chain-retraction time with $\tau_e = 2\tau_R$, τ_R being the longest Rouse relaxation time,[32,33] so that the entangled chains in the solutions are forced to orient and deform under the shear. The time evolutions of SALS intensity $\mathcal{I}_{\parallel}$ and $\mathcal{I}_{\perp}$, SALS patterns, and birefringence Δn_{x-z} shown in Figure 1B are found to be classified into the following four time regions t_1 to t_4 across the three critical times t_{c1} to t_{c3} as shown on top of part A and by broken vertical lines in part B.

(1) In region t_1 where time $t < t_{c1}$, t_{c1} being corresponding to the so-called "solvent-squeezing time" identified for the noncrystallizable polymer solutions,[18,35] the shear-enhanced SALS cannot be clearly discerned so that the sheared solution remains essentially homogeneous. This infers that the entangled chains are more or less uniformly deformed or oriented, hence causing an evolution of no excess scattering due to the shear flow but causing stress up-rise with time in the first stress overshoot process as discerned by the evolution of shear stress σ at $t <$ 1 s in Figure 1B and as found also for the noncrystallizable solutions.[18,48]

(2) In region t_2 where $t_{c1} < t < t_{c2}$, t_{c2} being the characteristic time for the formation of the demixed domains, the scattering pattern exhibit the so-called butterfly pattern with the butterfly wings oriented along the flow direction (*x*-axis) (pattern 1 in Figure 1B). The integrated intensity parallel to the flow direction, $\mathcal{I}_{\parallel}$, increased with t much more than that perpendicular to the flow direction, $\mathcal{I}_{\perp}$, which remains almost equal to $\mathcal{I}_{\perp}$ in the quiescent solution (see Figure 1B). This kind of the shear-enhanced scattering also supports that shear enhances the plane-wave-type concentration fluctuations with their wave vectors preferentially oriented along the flow direction in our observation of the scattering in the q_x−q_z plane, where q_j ($j = x$ or z) is the jth component of scattering vector **q**, though the wave vectors are expected to convect around *z*-axis[19] in the q_x−q_y plane. Under the imposed high $\dot{\gamma}$, much higher than τ_m^{-1} where τ_m is the longest rheological relaxation time, deformed, swollen, entangled chains cannot be relaxed through disentanglements.[18,34,49] Hence, they tend to recover more relaxed conformations and thereby favorable ones by squeezing solvents from the stretched entangled networks, as reported early for noncrystallizable polymer solutions.[35] The chain retraction coupled with the solvent squeeze[31] causes stress relaxation after the stress rise to a maximum value in the first stress overshoot process at $1 < t < 6$ s, as seen in σ vs t in Figure 1B.

We should note that thermal concentration fluctuations inherent in the solution give rise to density fluctuations in entanglement coupling points. Regions having more entanglements will bear larger stress and hence will squeeze more solvents than regions having fewer entanglements and thereby bearing less stress. This elastic effect and the stress imbalance between the two components having large and small mobilities develop shear-enhanced concentration fluctuations against osmotic pressure. Moreover, the elastic deformation of entangled networks is anisotropic, causing solvents be squeezed preferentially along the flow direction and hence generating the plane-wave-type concentration fluctuations as pointed out earlier for the noncrystallizable polymer solutions.[18,34] We should note that the same elastic effect is applied also to the solutions of crystallizable polymers. The scattering pattern 1 typical for the plane-wave concentration fluctuations is seen to be developed after the first stress overshoot when σ becomes close to the minimum value (Figure 1B).

In region t_3 where $t_{c2} < t < t_{c3}$, t_{c3} being the characteristic time for the string formation, $\mathcal{I}_{\perp}$ tends to drastically increase with t, and hence the dark streak of the butterfly pattern observed along the neutral direction tends to be obscured (see also pattern 2 in Figure 1B). The increase of the scattering along neutral direction is a nonlinear effect driven by shear and has been interpreted as a signature of the onset of phase separation and formation of demixed domains for the noncrystallizable solutions.[18,25,49] In this sense t_{c2} is the critical time for formation of the demixed domains even for the crystallizable solutions.

In region t_4 where $t > t_{c3}$, $\mathcal{I}_{\perp}$ tends to further increase with t, though the increase of $\mathcal{I}_{\parallel}$ saturates, giving rise to the trend of $\mathcal{I}_{\perp} > \mathcal{I}_{\parallel}$. The scattering pattern is composed of very sharp streak(s), preferentially oriented along the neutral direction (*z*-axis), and the butterfly pattern, oriented along the flow direction (*x*-axis), as shown in pattern 4 in Figure 1B. The streak

implies stringlike assemblies of demixed domains aligned parallel to the flow direction. As described earlier in the text, the stringlike assemblies have been found also for the entangled noncrystallizable polymer solutions.[23,48,50] The demixed domains as an internal structure of the string account for the butterfly pattern. It is important to note that the streaklike scattering pattern is fluctuating with time under the shear flow, giving rise to multiple streaks or single streak and to a change in their (or its) orientation around the neutral axis by about 20° arc at a maximum. The results imply that the strings exist under a dynamic equilibrium of growth and partial burst under the continuous shear flow and that they have a solidlike integrity or some rigidity (or some degree of crystallinity), hence being subjected to lateral forces originating from normal forces, which cause the orientational changes of the strings and thereby of the streak pattern with t. This time-dependent fluctuations of the streak pattern have never been observed in the case of the noncrystallizable solution, probably because the strings formed have a liquidlike or soft and flexible gel-like integrity.

Up to time region 3, birefringence Δn_{x-z} is almost zero or very small, so that the concentration fluctuations and the demixed domains are not accompanied by a remarkable chain orientation, polymer chains themselves being essentially in relaxed random coils even under the flow. The drastic change in Δn_{x-z} in region t_4 leads us to further classify this region into stage 1 and stage 2 across the vertical solid line as shown in part a. In an early stage of region t_4 (stage 1) Δn_{x-z} becomes slightly positive so that the strings in stage 1 have only a weak birefringence. However, it is striking to find a sharp increase of Δn_{x-z} in the beginning of stage 2, which reveals by itself that bundles of stretched chains interconnecting the demixed domains may start to be formed parallel to the string and hence to the flow direction, thereby the string starts to have a strong optical anisotropy, which may be a signature for the onset of the shear-induced crystallization. However, up to the stage 1 in time region 4 there are signatures only for the shear-induced concentration fluctuations and phase separation but no signature for the shear-induced crystallization.

References and Notes

(1) Mitsuhashi, S. *Bull. Text. Res. Inst.* (*J*) **1963**, *66*, 1–9.
(2) Pennings, A. J.; Kiel, A. M. *Kolloid Z. Z. Polym.* **1965**, *205*, 160–162.
(3) Keller, A.; Kolnaar, H. W. H. In *Processing of Polymer*; Meier, H. E. H., Ed.; VHC: New York, 1997; Vol. *18*, Chapter 4.
(4) Meerveld, J. V.; Peters, G. W. M.; Hutter, M. *Rheol. Acta* **2004**, *44*, 119–134.
(5) Somani, R. H.; Yang, L.; Zhu, L.; Hsiao, B. S. *Polymer* **2005**, *46*, 8587–8623.
(6) Baert, J.; Puyvelde, P. V.; Langouche, F. *Macromolecules* **2006**, *39*, 9215–9222.
(7) Ogino, Y.; Fukushima, H.; Matsuba, G.; Takahashi, N.; Nishida, K.; Kanaya, T. *Polymer* **2006**, *47*, 5669–5677.
(8) Fernandez-Ballester, F. Ph.D. Thesis, California Institute of Technology, 2007.
(9) Kimata, S.; Sakurai, T.; Nozue, Y.; Kasahara, T.; Yamaguchi, N.; Karino, T.; Shibayama, M.; Kornfield, J. A. *Science* **2007**, *316*, 1014–1017.
(10) Kanaya, T.; Matsuba, G.; Ogino, Y.; Nishida, K.; Shimizu, H. M.; Shinohara, T.; Oku, T.; Suzuki, J.; Otomo, T. *Macromolecules* **2007**, *40*, 3650–3654.
(11) Mykhaylyk, O. O.; Chambon, P.; Graham, R. S.; Fairclough, J. P. A.; Olmsted, P. D.; Ryan, A. J. *Macromolecules* **2008**, *41*, 1901–1904.
(12) Balzano, L.; Rastogi, S.; Peters, W. M. *Macromolecules* **2009**, *42*, 2088–2092.
(13) Hayashi, Y.; Matsuba, G.; Zhao, Y.; Nishida, K.; Kanaya, T. *Polymer* **2009**, *50*, 2095–2103.
(14) Yan, T.; Zhao, B.; Cong, Y.; Fang, Y.; Cheng, S.; Li, L.; Pan, G.; Wang, Z.; Li, X.; Bian, F. *Macromolecules* **2010**, *43*, 602–605.
(15) Mykhaylyk, O. O.; Chambon, P.; Impradice, C.; Fairclough, J. P. A.; Terrill, N. J.; Ryan, A. J. *Macromolecules* **2010**, *43*, 2389–2405.
(16) Doi, M.; Onuki, A. *J. Phys. II* **1992**, *2*, 1631.
(17) Onuki, A. *J. Non-Cryst. Solids* **1994**, *172*, 1151–1157.
(18) Hashimoto, T. *Bull. Chem. Soc. Jpn.* **2005**, *78*, 1–39.
(19) Helfand, E.; Fredrickson, G. H. *Phys. Rev. Lett.* **1989**, *62*, 2468–2471.
(20) Milner, S. T. *Phys. Rev. E* **1993**, *48*, 3674–3691.
(21) Onuki, A. *J. Phys., Condens. Matter* **1997**, *9*, 6119–6157.
(22) Hashimoto, T.; Fujioka, K. *J. Phys. Soc. Jpn.* **1991**, *60*, 356–359.
(23) Hashimoto, T.; Kume, T. *J. Phys. Soc. Jpn.* **1992**, *61*, 1839–1843.
(24) Wu, X.-L.; Pine, D. J.; Dixon, P. K. *Phys. Rev. Lett.* **1991**, *66*, 2408–2411.
(25) Saito, S.; Hashimoto, T.; Morfin, I.; Lindner, P.; Boue, F. *Macromolecules* **2002**, *35*, 445–459.
(26) Rietveld, J.; McHugh, A. J. *J. Polym. Sci., Polym. Lett. Ed.* **1983**, *21*, 919–926.
(27) Rietveld, J.; McHugh, A. J. *J. Polym. Sci., Polym. Phys. Ed.* **1985**, *23*, 2339–2358.
(28) McHugh, A. J.; Blunk, R. H. *Macromolecules* **1986**, *19*, 1249–1255.
(29) McHugh, A. J. In *Rheo-Physics of Multiphase Polymeric Systems*; Lyngaae-Jørgensen, J., Søndergaard, K., Eds.; Technomic Publishing: Lancaster, PA, 1995; Chapter 6.
(30) Murase, H.; Kume, T.; Hashimoto, T.; Ohta, Y. *Macromolecules* **2005**, *38*, 6656–6665.
(31) Endoh, M. K.; Takenaka, M.; Inoue, T.; Watanabe, H.; Hashimoto, T. *J. Chem. Phys.* **2008**, *128*, 164911−1–164911−12.
(32) Doi, M.; Edwards, S. F. *The Theory of Polymer Dynamics*; Oxford University Press: London, 1996.
(33) Osaki, K.; Inoue, T.; Isomura, T. *J. Polym. Sci., Part B: Polym. Phys. Ed.* **2000**, *38*, 1917–1925.
(34) Hashimoto, T. In *Soft Matter Characterization*; Borsali, R., Pecora, R., Eds.; Springer: Germany, 2008; Chapter 8.
(35) Saito, S.; Matsuzaka, K.; Hashimoto, T. *Macromolecules* **1999**, *32*, 4879–4888.
(36) Lieberwirth, I.; Loos, J.; Petermann, J.; Keller, A. *J. Polym. Sci., Part B: Polym. Phys.* **2000**, *38*, 1183–1187.
(37) It is a big surprise at first glance to note the similarity of the shear flow effects and the extensional flow effects on these structure evolutions, since these two flow geometries are known to have different effects on molecular orientation and stress evolution. However, we should note that the extensional flow field imposed on the fiber in the spinning line is complex because the extensional strain rate and stress depend on the distance Z from the spinneret along the spinning line, as expected from the Z dependence of birefringence, the fiber diameter, temperature, etc. (see for example refs 38 and 39). Consequently, it may be plausible that the elongational flow effects are still small in the position A (Z = 30 mm) and B (Z = 100 mm) near the spinneret, so that the birefringence and hence the chain orientation and stretching are negligibly small. This may explain the structure evolution at A and B similar to that shown in Figure 1A under the simple shear flow.
(38) Katayama, K.; Amano, T.; Nakamura, K. *Kolloid Z. Z. Polym.* **1968**, *226*, 125–134.
(39) Kim, K. H.; Cho, H. H.; Ito, H.; Kikutani, T. *J. Polym. Sci., Part B: Polym. Phys.* **2008**, *46*, 847–856.
(40) It may be puzzling why the chains bridging the demixed domains are under tension, while the chains inside the domains are still in random coil. Although the generalization of the effect or expectation deserves future works, at this moment we expect that the demixed domains are only partially draining with the solvent flow; hence, the chains inside being kept essentially random coil and that motions of the demixed domains as a whole in the solvent flow cause the chains bridging the domains be stretched and self-assembled into the bundles. The bundles of the stretched chains may further grow toward the inside of the domains
(41) Here LMW and UHMW polymer species serve as "solvents" and "polymers", respectively, in light of phase separation mediated by the dynamic asymmetry effects. However, one should note the following important facts: the "LMW solvents" can cocrystallize with the "UHMW polymers" in both shishs and kebabs,[7] while the solvent, decalin or paraffin, in polymer solutions never cocrystallizes with polymer.
(42) Hashimoto, T. *J. Polym. Sci., Part B: Polym. Phys.* **2004**, *42*, 3027–3062.
(43) de Gennes, P. G. *Scaling Concepts in Polymer Physics*, 1st ed.; Cornell University Press: Ithaca, NY, 1979.

(44) Murase, H.; Kume, T.; Hashimoto, T.; Ohta, Y.; Mizukami, T. *Macromolecules* **1995**, *28*, 7724–7729.
(45) Kume, T.; Asakawa, K.; Moses, E.; Matsuzaka, K.; Hashimoto, T. *Acta Polym.* **1995**, *46*, 79–85.
(46) Matsuzaka, K.; Hashimoto, T. *Rev. Sci. Instrum.* **1999**, *70*, 2387–2397.
(47) Murase, H. Doctoral Thesis, Kyoto University, 2005.
(48) Kume, T.; Hattori, T.; Hashimoto, T. *Macromolecules* **1997**, *30*, 427–434.
(49) Saito, S.; Hashimoto, T. *J. Chem. Phys.* **2001**, *114*, 10531–10543.
(50) Kume, T.; Hashimoto, T.; Takahashi, T.; Fuller, G. G. *Macromolecules* **1997**, *30*, 7232–7236.